Monthly Notices
of the
ROYAL ASTRONOMICAL SOCIETY

MNRAS **434,** 978–991 (2013)
Advance Access publication 2013 July 17

doi:10.1093/mnras/stt1014

Molecular gas in type 2 quasars at $z \sim 0.2$–0.3⋆

M. Villar-Martín,[1]† M. Rodríguez,[2] G. Drouart,[3,4] B. Emonts,[1,5] L. Colina,[1] A. Humphrey,[6] S. García Burillo,[7] J. Graciá Carpio,[8] P. Planesas,[7] M. Pérez Torres[2] and S. Arribas[1]

[1]*Centro de Astrobiología (INTA-CSIC), Carretera de Ajalvir, km 4, E-28850 Torrejón de Ardoz, Madrid, Spain*
[2]*Instituto de Astrofísica de Andalucía (CSIC), Glorieta de la Astronomía s/n, E-18008 Granada, Spain*
[3]*European Southern Observatory, Karl Schwarschild Str. 2, D-85748 Garching bei München, Gemany*
[4]*Institut dAstrophysique de Paris, 98bis boulevard Arago, F-75014 Paris, France*
[5]*CSIRO Astronomy and Space Science, Australia Telescope National Facility, PO Box 76, Epping NSW 1710, Australia*
[6]*Centro de Astrofisica, Universidade do Porto, Rua das Estrelas, P-4150-762 Porto, Portugal*
[7]*Observatorio Astronómico Nacional (OAN)-Observatorio de Madrid, Alfonso XII, 3, E-28014 Madrid, Spain*
[8]*Max-Planck-Institut für extraterrestrische Physik, Giessenbachstraβe 1, D-85748 Garching bei München, Germany*

Accepted 2013 June 5. Received 2013 June 1; in original form 2012 November 9

ABSTRACT

We present results of CO(1–0) spectroscopic observations of 10 Sloan Digital Sky Survey type 2 quasars (QSO2) at $z \sim 0.2$–0.3 observed with the 30-m IRAM radio telescope and the Australia Telescope Compact Array. We report five new confirmed CO(1–0) detections and one tentative detection. They have $L'_{\rm CO} \sim$ several $\times\ 10^9$ K km s^{-1} pc^2, while upper limits for the non-detections are $L'_{\rm CO} < 3\sigma =$ several $\times\ 10^9$ K km s^{-1} pc^2. This study increases the total number of QSO2 with CO measurements at $z \lesssim 1$ to 20, with a 50 per cent detection rate. The vast majority are at $z \sim 0.1$–0.4. Assuming a conversion factor $\alpha = 0.8$ M$_\odot$(K km s^{-1}pc^2)$^{-1}$, the implied molecular gas masses are in the range $M_{\rm H_2} \lesssim 4 \times 10^8$ to $\sim$5 $\times$ 10^9 M$_\odot$. We compare with samples of type 1 quasars (QSO1), luminous and ultraluminous infrared galaxies. We find no difference in the molecular gas content of QSO1 and QSO2 of a given infrared luminosity, although the QSO2 sample is affected by small number statistics. This result, if confirmed, is consistent with the unification model for quasars. QSO2 fall on the $L'_{\rm CO}$versus z, $L'_{\rm CO}$versus $L_{\rm FIR}$ and $\eta = \frac{L_{\rm FIR}}{L_{\rm CO}}$ versus $L_{\rm FIR}$ correlations defined by quasars at different z. The location of the QSO2 in these diagrams is discussed in comparison with samples of QSO1, luminous and ultraluminous infrared galaxies, and high-z submm sources. CO(1–0) has full width at half-maximum (FWHM) $\sim$ 180–370 km s^{-1} when detected, with a variety of kinematic profiles (single or double horned). In general, the CO line is narrower than [O III]λ5007, as observed in low-z QSO1, with FWHM$_{\rm [O\,III]}$/FWHM$_{\rm CO} \sim$ 1–2). This probably reveals different spatial sizes and/or geometry of the ionized and molecular phases and a higher sensitivity of the [O III] emission to non-gravitational motions, such as outflows. Considering the $z \sim 0.1$–0.4 range, where CO measurements for both QSO1 and QSO2 exist, we find no difference in FWHM$_{\rm CO}$ between them, although this result is tentative. In the unification scenario between QSO1 and QSO2, this suggests that the distribution of CO gas is not related to the obscuring torus.

Key words: galaxies: evolution – galaxies: interactions – quasars: general.

1 INTRODUCTION

It has been only in the last decade that radio quiet type 2 (i.e. obscured) quasars, generally known as 'type 2 quasars', have been discovered in large quantities at different wavelengths: X-ray (e.g. Szokoly et al. 2004), infrared (e.g. Stern et al. 2005; Martínez-Sansigre et al. 2006) and optical (Zakamska et al. 2003; Reyes et al. 2008). These authors have identified nearly 1000 type 2 quasars (QSO2 hereafter, versus QSO1 or type 1 quasars) at redshift $0.2 \lesssim z \lesssim 0.8$ in the Sloan Digital Sky Survey (SDSS; York et al. 2000) based on their optical emission line properties: narrow Hβ (full width at half-maximum, FWHM < 2000 km s^{-1}), high ionization emission lines characteristic of type 2 active

⋆Based on observations carried out with the IRAM 30-m radio telescope and the Australia Telescope Compact Array.

† E-mail: villarmm@cab.inta-csic.es

Table 1. The sample. Objects observed during runs A and B with the Institut de Radioastronomie Millimétrique (IRAM) 30-m radio telescope and with ATCA are separated by horizontal lines. z_{SDSS} (5) is the optical redshift derived from the [O III]λ5007 line using the SDSS spectra. D_L (6) is the luminosity distance in Mpc. t_{exp} (7) gives the total exposure time per source including calibrations. ν_{obs} (8) is the observed frequency of the CO(1–0) transition and rms (9) is the noise determined from channels with 16 MHz (∼50 km s^{-1}) spectral resolution. It is given in mK for the IRAM data and in mJy beam^{-1} chan^{-1} for the ATCA data.

(1) Object	(2) Run	(3) RA	(4) Dec.	(5) z_{SDSS}	(6) D_L (Mpc)	(7) Scale (kpc arcsec^{-1})	(8) t_{exp} (h)	(9) ν_{obs} (GHz)	(10) rms
SDSS J0831+07	A	08 31 30.3	+07 05 59.5	0.232	1147	3.7	5.2	93.6	0.4
SDSS J1044+06	A	10 44 26.7	+06 37 53.8	0.210	1025	3.4	6.2	95.3	0.3
SDSS J1106+03	A	11 06 22.0	+03 57 47.1	0.242	1204	3.8	3.9	92.8	0.4
SDSS J1301−00	A	13 01 28.8	−00 58 04.3	0.246	1227	3.8	6.0	92.5	0.4
SDSS J1344+05	A	13 44 18.7	+05 36 25.6	0.276	1399	4.2	6.2	90.3	0.2
SDSS J0028−00	B	00 28 52.87	-00 14 33.6	0.310	1601	4.5	9.2	87.1	0.2
SDSS J0103+00	B	01 03 48.58	+00 39 35.0	0.314	1625	4.6	8.0	87.7	0.3
SDSS J0236+00	B	02 36 35.06	+00 51 26.9	0.207	1009	3.4	6.5	95.5	0.2
SDSS 0025−10	ATCA	00 25 31.46	−10 40 22.2	0.303	1559	4.5	17.0	88.4	1.0
SDSS 0217−00	ATCA	02 17 58.18	−00 13 02.7	0.344	1808	4.9	7.5	85.8	2.2

galactic nuclei (AGN) and narrow-line luminosities typical of QSO1 ($L_{[O\,III]\lambda5007} \gtrsim 2 \times 10^8$ L$_\odot$).

Based on diverse studies it can be said that the host galaxies of QSO2 are often ellipticals with frequent signatures of mergers/interactions (Greene et al. 2009; Villar-Martín et al. 2011a, 2012; Bessiere et al. 2012). Very intense star formation activity is also frequently found (e.g. Lacy et al. 2007; Zakamska et al. 2008; Hiner et al. 2009). Ionized gas outflows are a ubiquitous phenomenon (Humphrey et al. 2010; Greene et al. 2011; Villar-Martín et al. 2011b). The optical continuum is sometimes polarized, revealing the presence of an obscured non-thermal continuum source (Vernet et al. 2001; Zakamska et al. 2005).

A fundamental piece of information is still missing: the molecular gas content of this class of objects has been very scarcely studied and it is not known whether the host galaxies of QSO2 contain abundant reservoirs of molecular gas. This gaseous phase can provide large amounts of fuel to form stars and feed the nuclear black hole. This gas is highly sensitive to the different mechanisms at work during galactic evolution (e.g. interactions and mergers). As such, it retains relic information about the global history of the systems.

CO, the strongest tracer of molecular gas, has been found in active galaxies (AGNs) at different z of similar AGN power as QSO2, i.e. QSO1 and powerful FRII (Fanaroff–Riley II) narrow-line radio galaxies (see Solomon & Vanden Bout 2005; Omont 2007; Miley & de Breuck 2008, for a global review). The inferred H_2 masses are in the range $M_{H2} = \alpha\ L'_{CO} \sim 10^8$-several $\times\ 10^9$ M$_\odot$ [where L'_{CO} is the CO(1–0) line luminosity and assuming $\alpha = 0.8$ M$_\odot$ (K km s^{-1} pc^2)$^{-1}$] (Downes & Solomon 1998)[1] at low z ($z \lesssim 0.1$; e.g. Evans et al. 2005; Bertram et al. 2007; Ocaña Flaquer et al. 2010) and several $\times\ 10^9$–10^{11} M$_\odot$ at $z \gtrsim 2$ (e.g. de Breuck et al. 2005; Emonts et al. 2011a; Ivison et al. 2011). The presence of CO has also been confirmed in several distant QSO2 at $z \gtrsim 3$, implying masses ∼several $\times\ 10^{10}$ M$_\odot$ (Marínez Sansigre et al. 2009; Polleta et al. 2011; Schumacher et al. 2012).

Many of these studies have focused at low ($z < 0.1$) and high redshift ($z > 2$), and frequently on luminous infrared sources. The intermediate-z range, which spans ∼60 per cent of the age of the Universe, an epoch of declining cosmic star formation rate (Hopkins & Beacom 2006), has remained almost practically unexplored until very recently. On this regard, two relevant papers have been published recently: on one hand, Xia et al. (2012) report CO detections in 17 out of 19 ultraluminous infrared QSO1 hosts (10^{12} L$_\odot \leq L_{IR}$, where L_{IR} is the infrared luminosity in the ∼8–1000 μm spectral range) at $z \sim 0.1$–0.2. They infer $M_{H_2} \sim$ (0.2–2.1) $\times\ 10^{10}$ M$_\odot$. On the other hand, Krips, Neri & Cox (2012, hereafter KNC12) have investigated for the first time the molecular gas content of 10 QSO2 at $z \sim 0.1$–0.4. According to our revised L_{IR} values (see Section 4.3), all but one have $L_{IR} \lesssim$ several $\times\ 10^{11}$ L$_\odot$. They confirm the detection of CO(1–0) in five sources and a tentative detection for a sixth. The derived gas masses are $M_{H_2} \sim$ (0.4–2.6) $\times\ 10^9$ M$_\odot$ for the detections and $\lesssim 2 \times 10^9$ M$_\odot$ for the four non-detections.[2]

We present here results on 10 more optically selected QSO2 at ∼0.2–0.3 based on data obtained with the 30-m Institut de Radioastronomie Millimétrique (IRAM) radio telescope and the Australian Telescope Compact Array (ATCA). We measure the CO(1–0) luminosities L'_{CO} and constrain the molecular gas masses and the infrared luminosities. These are compared with other samples of quasars, luminous infrared galaxies (LIRGs; with 10^{11} L$_\odot \leq L_{IR} < 10^{12}$ L$_\odot$), ultraluminous infrared galaxies (ULIRGs; 10^{12} L$_\odot \leq L_{IR}$) and high-z submm sources.

We assume $\Omega_\Lambda = 0.7$, $\Omega_M = 0.3$, $H_0 = 71$ km s^{-1} Mpc^{-1}.

2 THE SAMPLE

The sample consists of 10 radio quiet ($P_{5\,GHz} < 10^{31}$ erg s^{-1} Hz^{-1} sr^{-1}; Miller, Peacock & Mead 1990) SDSS QSO2 at $z \sim 0.2$–0.34 (Table 1) selected from the original sample of Reyes et al. (2008) and Zakamska et al. (2003) (see these papers for a detailed description of the selection criteria). These are objects with narrow (FWHM $\lesssim$ 1000 km s^{-1}) forbidden and permitted emission lines without underlying broad components, with line ratios characteristic of a non-stellar ionizing radiation and [O III] λ5007 luminosities typical of QSO1.

The IRAM sample consists of eight SDSS QSO2. No bias was applied regarding the host galaxy properties or the infrared (IR) luminosities. The only criteria were that they were observable with

[1] Recent results imply $\alpha = 0.6 \pm 0.2$ (Papadopoulos et al. 2012).

[2] For coherence with the rest of this work, we have recalculated M_{H_2} for KNC12 sample assuming a conversion factor $\alpha = 0.8$ M$_\odot$ (K km s^{-1} pc^2)$^{-1}$ instead of the 4.8 value used by those authors. We have also recalculated their upper limits using the FWZI, instead of the FWHM (Section 3.3).

Table 2. The luminosity (2) of the [O III]λ5007 line (Reyes et al. 2008) is given in log and relative to $L_\odot$. L'_{CO} (3) is in units of $\times 10^9$ K km s^{-1} pc^2. A conversion factor $\alpha = 0.8$ $M_\odot$ (K km s^{-1} pc^2)$^{-1}$ has been assumed to calculate the molecular gas mass (4), with $M_\odot = \alpha \times L'_{CO}$. $V_{CO-[O\,III]}$ is the velocity shift of the CO(1–0) line relative to z_{SDSS}. The two values of FWHM$_{CO}$ (5) and $V_{CO-[O\,III]}$ (7) shown for SDSS J1344+05 and SDSS J0025−10 correspond to the two spectral components identified in the double horned CO line profile. SDSS J0236+00 is marked with a question mark '?' because the detection is only tentative (see Section 5.1). The [O III]λ5007 FWHM (6) has been measured using the SDSS spectra. Columns (8) and (9) give the infrared (∼8–1000 μm) and far-infrared (40–500 μm) luminosities in units of $\times 10^{11}$ $L_\odot$. L_{IR} and L_{FIR} could not be constrained for SDSS J0028−00 (see Section 4.3).

(1) Object	(2) $\log(\frac{L_{[O\,III]}}{L_\odot})$	(3) L'_{CO} ($\times 10^9$)	(4) M_{H2} ($\times 10^9$ $M_\odot$)	(5) FWHM$_{CO}$ (km s^{-1})	(6) FWHM$_{[O\,III]}$ (km s^{-1})	(7) $V_{CO-[O\,III]}$ (km s^{-1})	(8) L_{IR} $\times 10^{11}$ $L_\odot$	(9) L_{FIR} $\times 10^{11}$ $L_\odot$
SDSS J0831+07	8.52	6.5 ± 1.0	5.2 ± 0.9	370 ± 60	685 ± 10	20 ± 30	≤4	≤ 2.6
SDSS J1044+06	8.17	<2.0	<1.6	–	1050 ± 20	–	≤2.3	≤1.6
SDSS J1106+03	9.02	<4.3	<3.4	–	545 ± 10	–	8.7 ± 0.6	5.7 ± 0.5
SDSS J1301−00	9.14	<4.1	<3.3	–	760 ± 10	–	≤9.5	≤6.5
SDSS J1344+05	8.12	2.4 ± 0.6	1.9 ± 0.5	180 ± 30	500 ± 15	-310 ± 50	≤5.5	≤5
		3.8 ± 0.6	3.0 ± 0.4	220 ± 30		-20 ± 30		
SDSS J0028−00	8.43	6 ± 1	5 ± 1	300 ± 100	330 ± 10	60 ± 30	–	–
SDSS J0103+00	8.31	6 ± 1	4.8 ± 0.9	280 ± 50	355 ± 10	8 ± 30	≤18	≤12
SDSS J0236+00?	9.20	5.0 ± 0.5	1.7 ± 0.4	220 ± 40	800 ± 20	-1670 ± 30	4.2 ± 1.5	2.8 ± 0.1
SDSS 0025−10	8.73	4.3 ± 0.9	3.4 ± 0.7	140 ± 25	440 ± 10	-155 ± 25	$11.0 \pm 3 \pm$	7.8 ± 2.2
		3.1 ± 0.9	2.5 ± 0.7	80 ± 40		-5 ± 20		
SDSS 0217−00	8.81	<6.2	<5.0	–	985 ± 15	–	12.0 ± 0.8	8.7 ± 0.6

the IRAM radio telescope and with $z \lesssim 0.3$, so that the CO(1–0) transition falls within the EMIR E090 band. This transition is the least dependent on the excitation conditions of the gas, which is crucial for deriving reliable estimates of the total molecular gas content, including the wide spread, low-density gas that may be sub-thermally excited (e.g. Papadopoulos et al. 2001; Carilli et al. 2010).

Two more QSO2 at similar z were observed with ATCA (SDSS J0025−10 and SDSS J0217−00), which were specifically selected for being luminous IR sources (with *IRAS* counterparts) and for showing interesting features such as being strong mergers. These two systems were studied in detail by Villar-Martín et al. (2011a,b) based on deep optical imaging and spectroscopy obtained with the Faint Object FOcal Reducer and low dispersion Spectrograph (FORS2) on the Very Large Telescope (VLT). A detailed study of the CO(1–0) spatial distribution in SDSS J0025−10 based on the ATCA data can be found in Villar-Martín et al. (2013).

The luminosity of the [O III] λ5007 line, $L_{[O\,III]}$, has been proposed as a proxy for the AGN power (Heckman et al. 2004) and a potential discriminant between Seyferts and quasars. This is specially useful for type 2 objects for which the optical colours result from a complex mixture of the host galaxy continuum and AGN related sources (e.g. Vernet et al. 2001). All but two objects in our sample have $\log(\frac{L_{[O\,III]}}{L_\odot}) > 8.3$ (Table 2, Column 2) which is the lower limit applied by Reyes et al. (2008) to select quasars versus Seyferts. The two remaining objects have values ∼8.1–8.2, i.e. a factor of ≤1.5 below this limit. However, taking into account that reddening has been ignored and the fact that [O III] is partially obscured in type 2 AGNs (di Serego Alighieri et al. 1997), we consider these two objects as QSO2 as well. It must also be kept in mind that the relation between the [O III]λ5007 and bolometric luminosity for quasars has a significant scatter, resulting in a somewhat arbitrary separation between quasars and Seyferts (e.g. Zakamska et al. 2003).

We will refer frequently throughout the paper to the QSO2 sample studied by KNC12. All but two objects are from the original sample of 24 μm selected galaxies observed with the *Spitzer* infrared spectrograph for the 5 millijanksy Unbiased Spitzer Extragalactic Survey (5MUSES) (Wu et al. 2010, see also Lacy et al. 2007). The other two quasars are from the QSO2 SDSS sample of Zakamska et al. (2003).

3 OBSERVATIONS

3.1 IRAM observations

The observations were obtained during two different observing runs A and B in 2012 February and August, respectively, with the IRAM 30-m telescope at Pico Veleta, Spain. The EMIR receiver was tuned to the redshifted frequencies of the CO line, using the optical SDSS redshift z_{SDSS} for each object (see Table 1). The observations were performed in the wobbler switching mode with a throw of 120 arcsec (run A) or 50 arcsec (run B), in order to ensure flat baselines. We observed both polarizations (H and V) using as a backend the WILMA autocorrelator that produced an effective total bandwidth of 4 GHz with a (Hanning-smoothed) velocity resolution of 16 MHz or ∼50 km s^{-1}.

For run A the observing conditions were good precipitable water vapour (pwv ≤ 4 mm). For run B the conditions were variable with pwv in the range ∼3–10 mm. The system temperatures were in the range T_{sys} ∼ 76–114 K for run A and ∼102–106 K for run B. The total integration time and the rms for all sources are specified in Table 1.

The temperature scale used is in main beam temperature T_{mb}. At 3 mm the telescope half-power beam width is 29 arcsec. The main-beam efficiency is $\eta_{mb} = T_A^*/T_{mb} = 0.81$. A factor $S/T_A^* = 5.9$ Jy K^{-1} was applied to obtain the flux in mJy beam^{-1} units.

The pointing model was checked against bright, nearby calibrators for every source, and every 1.6 h for long integrations; it was found to be accurate within 5 arcsec. Calibration scans on the standard two load system were taken every 8 min. The focus was checked after sunrise, after sunset and every six hours.

The off-line data reduction was done with the CLASS program of the GILDAS software package (Guilloteau & Forveille 1989), and involved only the subtraction of (flat) baselines from individual integrations and the averaging of the total spectra.

3.2 ATCA observations

The observations of SDSS J0025−10 and SDSS J0217−00 were performed during 2012 August 2–7 with the Australia Telescope Compact Array (ATCA), a radio interferometer in Narrabri, Australia. Observations were done in the compact hybrid H75 array configuration (with baselines ranging from 31 to 89 m). Two 2 GHz bands with 1 MHz channel resolution were centred on the redshifted frequency of the CO(1–0) line for each object (88.4 GHz for SDSS J0025−10 and 85.8 GHz SDSS J0217−00; Table 1), resulting in a velocity coverage of 7000 km s^{-1} and maximum resolution of 3.5 km s^{-1}. At 88 GHz, the primary beam of the telescope is 32 arcsec. Observations were done under good weather conditions, with typical system temperatures of 400–650 K and atmospheric seeing fluctuations <150 μm for SDSS J0025−10 and <300 μm for SDSS J0217−00 (see Middelberg, Sault & Kesteven 2006). The total on-source integration time was 17 h for SDSS J0025−10 and 7.5 h for SDSS J0217−00.

The phases and bandpass were calibrated every 7.5 min with a short (∼2 min) scan on the nearby bright calibrators PKS 0003−066 (SDSS J0025−10) and PKS J0217+0144 (SDSS J0217−00). Atmospheric amplitude variation were calibrated every 30 min using a paddle scan, and telescope pointing was updated every hour, or every time the telescope moved >20° on the sky. For absolute flux calibration, Uranus was observed close to our target source, resulting in an absolute flux calibration accuracy of 20 per cent.

The off-line data reduction was done with the MIRIAD software. Bad data (including data with internal interference or shadowing of an antenna) were discarded. For the data reduction we followed Emonts et al. (2011b), noting that atmospheric opacity variations were corrected by weighting the data according to their 'above atmosphere' (i.e. paddle-corrected) system temperature. After Fourier transformation, we obtained data cubes with robust weighting +1 (Briggs 1995).

No 88/85 GHz radio continuum was detected in these data cubes down to a 5σ limit of 0.5 mJy for SDSS J0025−10 and 0.9 mJy for SDSS J0217−00. The synthesized beam-size of the J0025−10 data is 6.30 × 4.39 arcsec^2 (PA −85.°3) and that of SDSS J0217−00 data is 6.64 × 5.30 arcsec^2 (PA −70.°7). The spectra presented in this paper were extracted at the location of the quasar host galaxies, binned by five channels and subsequently Hanning smoothed to a velocity resolution of 50 km s^{-1}, yielding a noise level of 1.0 and 2.2 mJy beam^{-1} chan^{-1} for SDSS J0025−10 and SDSS J0217−00, respectively. We also imaged the spatial distribution of the CO(1–0) detected in SDSS J0025−10. This is presented in Villar-Martín et al. (2013).

4 ANALYSIS

4.1 The comparison samples

In the following sections (in particular Fig. 3) we will perform a comparative study between QSO2 and QSO1, LIRGs, ULIRGs and submillimetre sources at different z.

We describe here briefly these samples and the symbol/colour code used in Fig. 3 for their representation. For coherence with our work, upper limits have been recalculated using full width at zero intensity FWZI, instead of FWHM whenever possible.

(i) QSO1 (blue symbols)

(a) non-ULIRG QSO1 at $z \lesssim 0.2$ (blue open circles, from Evans et al. 2001, 2006; Scoville et al. 2003; Pott et al. 2006; Bertram et al. 2007).

(b) ULIRG QSO1 at $z \sim 0.1$–0.3 (blue solid circles; Xia et al. 2012).

(c) ULIRG QSO1 at $z \sim 0.2$–1 (blue solid squares; Combes et al. 2012, 2011).

(d) $z \gtrsim 2$ QSO1 (blue crosses; Cox et al. 2002; Carilli et al. 2002; Walter et al. 2004; Krips et al. 2005; Riechers, Walter & Carilli 2006; Gao et al. 2007; Maiolino et al. 2007; Coppin et al. 2008; Wang et al. 2010, 2011; Riechers, Walter & Frank 2009a; Riechers et al. 2009b).

(ii) QSO2 (green symbols)

(a) 10 QSO2 from this work (green solid circles)

(b) 10 QSO2 from KNC12 (green solid squares)

Unlike for QSO1, ULIRG-QSO2 are not included because as we shall see in Section 4.3, the three most luminous QSO2 have $L_{\rm IR}$ in the LIRG–ULIRG transition regime. All other QSO2 at intermediate z have $L_{\rm IR}$ in the LIRG regime or below.

(c) High-z QSO2 (green solid triangles; Aravena et al. 2008; Marínez Sansigre et al. 2009; Yan et al. 2010; Polleta et al. 2011; Lacy et al. 2011).

(iii) ULIRGs (no quasars included) and submm sources with no obvious evidence for an AGN (red symbols)

(a) $0.04 \lesssim z < 0.2$ ULIRGs (red solid diamonds; Graciá Carpio et al. 2008). This sample consists of star-forming galaxies and AGN (Seyfert 1, Seyfert 2 and Liners).

(b) $0.2 \lesssim z \lesssim 0.6$ ULIRGs (red solid triangles, Combes et al. 2011, 2012). This sample consists of star-forming galaxies and AGN (Seyfert 1, Seyfert 2 and Liners).

(c) $z \gtrsim 2$ submm sources with no obvious evidence of an AGN (Solomon, Downes & Radford 1992; Neri et al. 2003; Smail, Smith & Ivison 2005; Weiss et al. 2005; Gao et al. 2007; Daddi et al. 2009; Ivison et al. 2011; Bothwell et al. 2013). The luminosities have been corrected for magnification in lensed sources.

(iv) $z \lesssim 0.05$ LIRGs (orange crosses, Graciá Carpio et al. 2008; García Burillo et al. 2012). The LIRG sample consists of star-forming galaxies and AGN (Seyfert 1, Seyfert 2, Liners), but not quasars.

4.2 Calculation of $L'_{\rm CO}$ and $M_{\rm H_2}$

A major part of the results presented in this paper is based on the CO(1–0) line luminosities $L'_{\rm CO}$ and the far-infrared luminosity $L_{\rm FIR}$ measured between ∼40 and 500 μm rest frame. To infer them, different methods and observables have been used for different samples and redshifts. We explain in detail in this and next section the methodology applied.

$L'_{\rm CO}$ in K km s^{-1} pc^2 is calculated as (Solomon & Vanden Bout 2005):

$$L'_{\rm CO} = 3.25 \times 10^7 \left(\frac{S_{\rm CO}\Delta V}{\rm Jy\,km\,s^{-1}}^{-1}\right) \left(\frac{D_{\rm L}}{\rm Mpc}\right)^2 \left(\frac{\nu_{\rm rest}}{\rm GHz}\right)^{-2} (1+z)^{-1}$$

where $I_{\rm CO} = S_{\rm CO}\,\Delta V$ is the integrated CO(1–0) line intensity in Jy km s^{-1}, $D_{\rm L}$ is the luminosity distance in Mpc (Table 1) and $\nu_{\rm rest} = 115.27$ GHz is the rest-frame frequency of the CO(1–0) transition.

For the non-detections (i.e. $I_{\rm CO} < 3\sigma$), we calculate the upper limit as (Sage 1990):

$$I_{\rm CO} < 3\sigma_n \sqrt{\rm FWZI \times \Delta v}\ \ {\rm Jy\,km\,s^{-1}},$$

where $\Delta v = 50$ km s^{-1} is the channel width and σ_n is the channel-to-channel rms noise of the spectrum in Jy. We have assumed a

typical FWZI = 870 km s^{-1}, using the median value of our *FWZI* and KNC12 measurements.

Different CO transitions are observable at different z. In order to extrapolate to the CO(1–0) transition for all objects, we have assumed a constant effective brightness temperature for the different transitions (thus, $\frac{L'_{CO(J=n+1\rightarrow n)}}{L'_{CO(J=n\rightarrow n-1)}} = 1$). This is usually assumed for low-z studies, where the gas is likely to be optically thick and thermally excited (e.g. Combes et al. 2012; but see also Papadopoulos et al. 2012). At high z the uncertainties on the CO excitation are larger. Some works suggest that thermal excitation is a reasonable assumption both for quasars (Riechers 2011) and for submm sources (Weiss et al. 2005; Aravena et al. 2008), while others rather suggest sub-thermal excitation (Carilli et al. 2010). If this were the case, we would be underestimating the L'_{CO} by a factor of ∼2–4 for the high-z sources. This and other uncertainties such as the accuracy of the magnification factor in confirmed lensed objects are likely to contribute to the data scatter at high z. However, this will have a small impact on our conclusions since the scatter of the L'_{CO} values at a given z is also very large, spanning ∼2 orders of magnitude considering all object classes.

To estimate the molecular gas masses we use the standard conversion formula (Solomon & Vanden Bout 2005):

$$\frac{M_{H_2}}{M_\odot} = \frac{\alpha}{M_\odot\ (\mathrm{K\ km\ s^{-1}\ pc^2})^{-1}}\ \frac{L'_{CO}}{\mathrm{K\ km\ s^{-1}\ pc^2}}.$$

For the purpose of comparison with other works, we have assumed $\alpha = 0.8\ M_\odot\ (\mathrm{K\ km\ s^{-1}\ pc^2})^{-1}$, which has been frequently adopted for ULIRGs and active galaxies.

4.3 Calculation of L_{FIR}

We plan to investigate the location of our QSO2 in the L'_{CO} versus L_{FIR} diagram, relatively to other samples. Thus, L_{FIR} values are required for all objects. Alternatively L_{IR} can be used, but L_{FIR} is more generally available for the different samples in the literature. Also, it maps cooler dust and in principle it is a more reliable tracer of the dust emission induced by starburst heating. Finally, L_{FIR} is less dependent on orientation than L_{IR}, due to the higher sensitivity of the mid-infrared luminosity ($L_{MIR} = L_{IR} - L_{FIR}$) to obscuration (Drouart et al. 2012).

To constrain L_{FIR} for our QSO2 we have fitted the spectral energy distribution (SED) for the four objects with Wide-Field Infrared Explorer (WISE) (3.3, 4.6, 11.6, 22.1 μm) and *IRAS* (60 and/or 100 μm) photometric measurements: SDSS J1106+03, SDSS J0236+00 and SDSS J0025−10, SDSS J0217−00 (see Figs A1 and A2 in the Appendix). Optical and near-infrared photometry have not been used, since these bands are known to be a complex mixture of stellar and AGN-related components (e.g. scattered/transmitted AGN light, nebular continuum). To build the SEDs we used the *Spitzer* Wide-area Infrared Extragalactic (SWIRE) template library (Polletta et al. 2007) which contains 25 templates including ellipticals, spirals, starbursts, type 2 and type 1 AGNs and composite starburst + AGN. The results are shown in Table 2. The uncertainties are dominated by the range of templates able to reproduce the data. SDSS J0028−00 has been excluded in this analysis because an unrelated galaxy very close in projection confuses the IR photometry.

For the remaining five objects in our sample, *IRAS* upper limits are available and WISE photometry: SDSS J0831+07, SDSS J1044+06, SDSS J1301−01, SDSS J1344+05, SDSS J0103+00. Only upper limits on L_{IR} and L_{FIR} can be obtained for these objects by fitting the SED (Table 2).

Applying the same method, we have recalculated L_{FIR} and L_{IR} for the five objects in KNC12 with both mid- and far-IR photometric data to alleviate the large uncertainties affecting their values (Table 3). For four more objects L_{IR} is available from Wu et al. (2010) and Zakamska et al. (2008). For the remaining quasar, L_{IR} was constrained from the 24 μm luminosity using the equations proposed by Wu et al. (2010). To constrain L_{FIR} for these quasars, we have estimated a conversion factor $\xi = \frac{L_{IR}}{L_{FIR}}$ appropriate for QSO2. For this, we have used the nine QSO2 with both L_{IR} and L_{FIR} values available in both samples. They show very similar ξ in the range 1.4–1.7, with a median value of 1.5, that we assume for ξ. The final revised L_{IR} and L_{FIR} values for KNC12 QSO2 are shown in Table 3. We have applied the same conversion factor to high z QSO2 with only L_{IR} available (Polletta et al. 2011).

To estimate a conversion factor $\xi' = \frac{L_{IR}}{L_{FIR}}$ appropriate for QSO1, we have collected the *IRAS* flux measurements at 12, 25, 60 and 100 μm for nearby type 1 quasars with the four measurements published (∼17 objects in Sanders et al. 1989). We find that $\xi\prime$ is in the range ∼2.0–3.3, with a median value of 2.96, which we therefore assume to estimate L_{FIR} for those few QSO1 with no available L_{FIR}.

The low ξ values we have measured for $z < 0.4$ QSO2 are consistent with the unification scenario of QSO1 and QSO2. They suggest

Table 3. The KNC12 sample.

Object	z	L'_{CO} ($\times 10^9$)	L_{IR} ($\times 10^{11}$)	L_{FIR} ($\times 10^{11}$)
SWIRE2 J021638.21−042250.8	0.304	2.3	2.0 ± 0.5^a	1.2 ± 0.2^a
SWIRE2 J021909.60−052512.9	0.099	0.7	0.8 ± 0.1^a	0.55 ± 0.05^a
SWIRE2 J021939.08−051133.8	0.150	1.7	0.95 ± 0.05^a	0.6 ± 0.1^a
SWIRE2 J022306.74−050529.1	0.330	3.3	6 ± 2^b	4.0 ± 1.3^c
SWIRE2 J022508.33−053917.7	0.293	≤2.2	1.5 ± 0.5^a	1.2 ± 0.2^a
SDSS J092014.11+453157.3	0.403	≤2.8	8.2^d	5.5^c
SDSS J103951.49+643004.2?	0.402	2.1	13.0^d	8.7^c
SSTXFLS J171325.1+590531	0.126	≤0.5	0.23 ± 0.03^e	0.15 ± 0.02^c
SSTXFLS J171335.1+584756	0.133	0.5	1.0 ± 0.2^a	0.7 ± 0.2^a
SSTXFLS J172123.1+601214	0.325	≤1.8	4.5 ± 1.5^b	3 ± 1^c

Notes. L'_{CO} from table 4 in KNC12. L_{IR} and L_{FIR} values: [a]derived with our SED fitting technique; [b]inferred from equations (A22)– (A24) in Wu et al. (2010). The errors account for the three scenarios described by the equations, but not for the scatter in each formula; [c]L_{FIR} obtained from $L_{FIR} = L_{IR}/\xi$, with $\xi = 1.5$ (see text); [d]from Zakamska et al. (2008). No errors quoted by the authors; [e]from table 2 in Wu et al. (2010). A question mark (?) indicates a tentative CO(1–0) detection.

that the MIR emission, which is expected to be emitted by the hottest dust in the inner faces of the obscuring torus (Drouart et al. 2012), is partially obscured. This is consistent with Hiner et al. (2009), who found that QSO1 have less far-IR emission on average when compared to QSO2 matched in mid-infrared luminosity. Similarly, the authors propose that this difference is due to orientation.

We have used a conversion factor $\xi_* = \frac{L_{\rm IR}}{L_{\rm FIR}} = 1.3$ appropriate for high-z submm (Ivison et al. 2011) sources with no evidence for an AGN. This is the median value inferred for the sample of $z \lesssim 0.2$ ULIRGs of Graciá Carpio et al. (2008). It is consistent with works which show that most non-active galaxies have $\xi_* \sim 1.3$ (Pott et al. 2006) over several orders of magnitude of $L_{\rm IR}$.

5 RESULTS AND DISCUSSION

5.1 $L'_{\rm CO}$ and $M_{\rm H_2}$

CO(1–0) detection (S/N≥3 over the integrated line profile) is confirmed in five out of the 10 quasars observed (Figs 1 and 2 and Table 2): SDSS J0831+07, SDSS J1344+05, SDSS J0028−00,

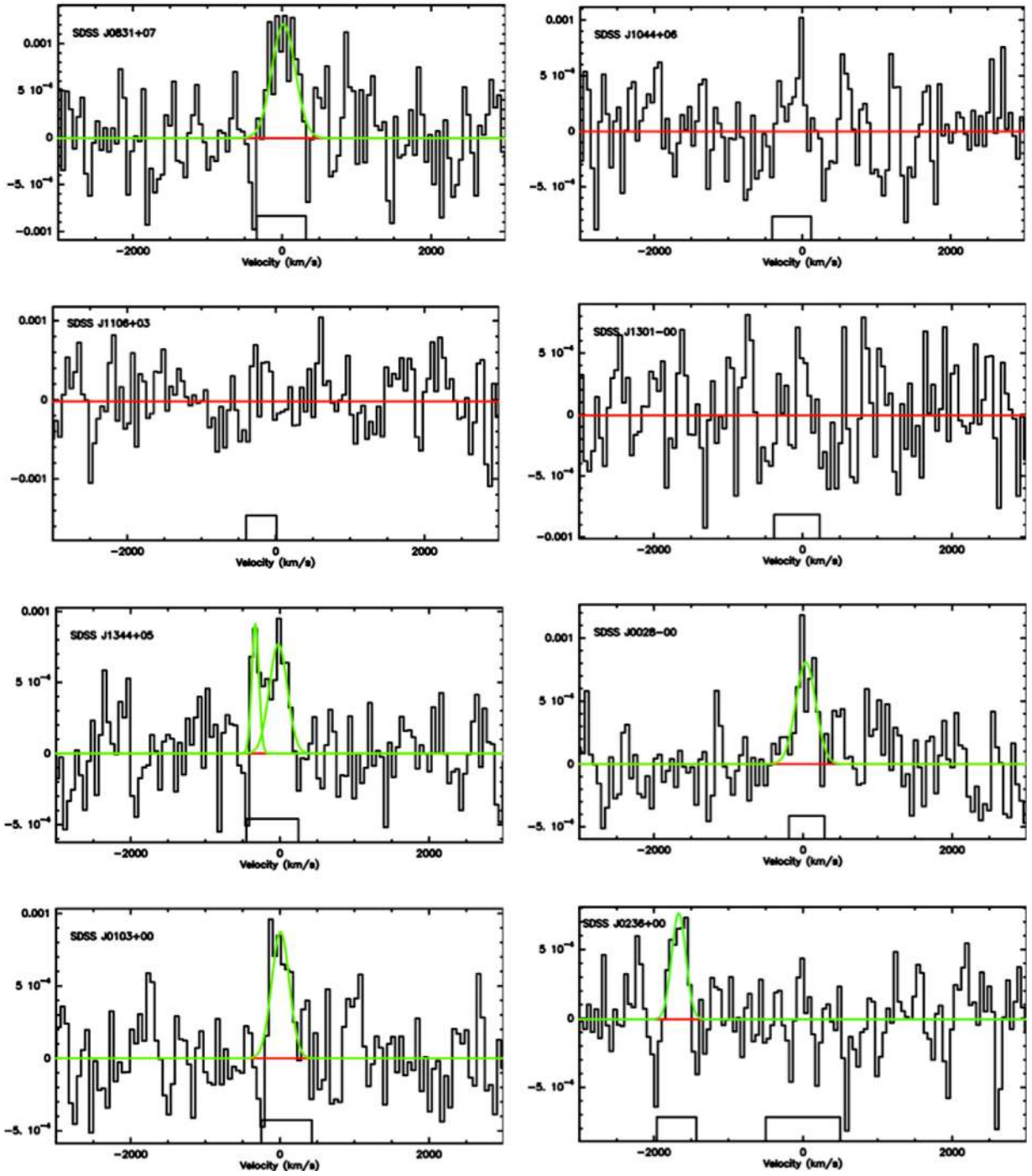

Figure 1. CO(1–0) spectra of the IRAM sample. The zero velocity corresponds to the optical redshift $z_{\rm SDSS}$, as derived from [O III]λ5007. Fits of the line profile are shown with green lines for objects with detections or tentative (SDSS J0236+00) detections. The vertical axis shows T_A^* in K.

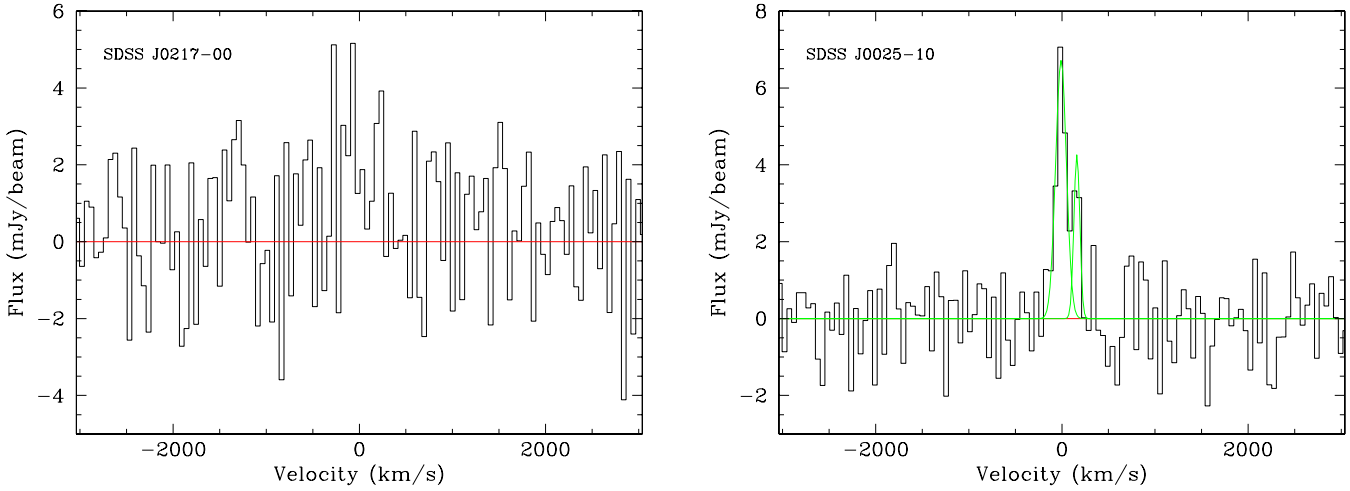

Figure 2. CO(1–0) spectra of the two QSO2 observed with ATCA. Zero velocity as Fig. 1. Flux units in mJy beam^{-1}. Notice the double horned line profile of SDSS J0025−10.

SDSS J0103+00 and SDSS J0025−10. For a sixth object, SDSS J0236+00, we claim a tentative detection. The spectrum shows an emission line feature detected at 5σ level with FWHM = 220 ± 40 km s^{-1}. The shift in velocity relative to [O III]λ5007 is very large, with $V_{\rm CO-[O\,III]} = -1670 \pm 30$ km s^{-1} compared with <100 km s^{-1} measured for the other objects (see Column 12 in Table 1). A similar case was discussed by KNC12, although these authors can confirm that the CO emission is close to the spatial position of the QSO2 radio emission.

The *K*-band image of SDSS J0236+00 shows a disturbed morphology (Stanford et al. 2000). There is an object located at ∼5 arcsec (∼17 kpc) NW of the quasar (thus, well within the 29 arcsec telescope beam) with a hint of a tidal tail connecting it to the quasar. However, the z is unknown and it could be an unrelated source. In any case, even if this object is confirmed to be a companion, it seems unlikely that the CO line is associated with it, since the velocity shift is rather extreme for a galaxy pair (Patton et al. 2000). If the CO emission line feature is not associated with the quasar, we estimate an upper limit for $L'_{\rm CO} < 3\sigma = 3 \times 10^9$ K km s^{-1} pc^2.

All six quasars with confirmed or tentative CO detection have $L'_{\rm CO} \sim$ several $\times 10^9$ K km s^{-1}pc^2 (Table 2), while upper limits for the four non-detections are $L'_{\rm CO} < 3\sigma =$ several $\times 10^9$ K km s^{-1} pc^2. The broad-band width (±5000 km s^{-1} relative to the optical redshift) of the spectra ensures that the non-detections are real, rather than due to a shift in velocity of the molecular gas emission out of the observed spectral band. For comparison, the objects with definite CO detections in KNC12 sample ($z \sim 0.1$–0.4) have $L'_{\rm CO}$ in the range (0.5–3.3) $\times 10^9$ K km s^{-1} pc^2, while the non-detections have in all cases $L'_{\rm CO} < 3\sigma \sim 3 \times 10^9$ K km s^{-1} pc^2.

The implied molecular gas masses for our sample assuming $\alpha = 0.8\,{\rm M}_\odot\,({\rm K\,km\,s^{-1}\,pc^2})^{-1}$ are ∼(2–6) $\times 10^9$ M$_\odot$ for the quasars with detections and $\lesssim$several $\times 10^9$ M$_\odot$ for the non-detections. Masses $\lesssim 2 \times 10^9$ M$_\odot$ are derived for all but one QSO2 in KNC12. Their objects have in general lower IR luminosities which can also explain the lower $M_{\rm H_2}$ (see Section 4.2). For comparison, the Milky Way contains ∼(2–3) $\times 10^9$ M$_\odot$ of molecular gas (Combes 1991).

We conclude that the 20 QSO2 observed so far at $z \sim 0.1$–0.4 (KNC12 and our sample) have CO(1–0) luminosities in the range $L'_{\rm CO} \lesssim 5 \times 10^8$–$6.5 \times 10^9$ L$_\odot$ and $M_{\rm H_2} \lesssim 4 \times 10^8$–$5 \times 10^9$ M$_\odot$. Most of these QSO2 have total IR luminosities $<10^{12}$ L$_\odot$. Larger molecular gas reservoirs $>10^{10}$ M$_\odot$ will probably be found when $L_{\rm IR} >$ several $\times 10^{12}$ L$_\odot$ QSO2 are investigated. We next compare with other QSO samples, as well as LIRGs and ULIRGs.

5.2 $L'_{\rm CO}$ versus z, $L'_{\rm CO}$ versus $L_{\rm FIR}$ and $\frac{L_{\rm FIR}}{L_{\rm CO}}$ versus $L_{\rm FIR}$

$L'_{\rm CO}$ is known to correlate with both z and $L_{\rm FIR}$ for different types of galaxies, active and non-active (e.g. Solomon & Vanden Bout 2005). These apparent correlations reflect partially a selection bias since at the highest z we are sensitive only to the most luminous CO and IR emitters. However, this is unlikely the whole story and a combination of the steep decline at the highest luminosities of the $L'_{\rm CO}$ and $L_{\rm FIR}$ luminosity functions and the evolution of such functions with z are also likely to play a role (Keres, Yun & Young 2003; Pérez González et al. 2005; Lagos et al. 2011). On the other hand, some works suggest that distant star-forming galaxies were indeed much more molecular-gas rich (e.g. Daddi et al. 2010; Tacconi et al. 2010).

As in other galaxy types, the $L'_{\rm CO}$ versus $L_{\rm FIR}$ correlation also reflects that more intense star formation is associated with larger contents of molecular gas. The interpretation is not so clear cut in quasars given the uncertain contribution of the AGN to the dust heating. Although $L_{\rm FIR}$ is less affected than $L_{\rm IR}$ by this effect due to the dominant contribution of the AGN to $L_{\rm MIR}$ (see Section 4.3), some contamination cannot be totally ruled out (e.g. Hiner et al. 2009).

We show $L'_{\rm CO}$ versus z and $L'_{\rm CO}$ versus $L_{\rm FIR}$ in Fig. 3.[3] Quasars only (blue and green symbols) are included on the left panels (A and B). LIRGs (orange symbols) and ULIRGs and high-z submm sources with no evidence for an AGN (both represented with red symbols) are added on the right-hand panels (C and D). The well-known $L'_{\rm CO}$ versus z and $L'_{\rm CO}$ versus $L_{\rm FIR}$ correlations for quasars are clearly appreciated in panels (A) and (B), respectively.

Quasar activity is clearly triggered in systems spanning a range of more than 4 orders of magnitude both in infrared and in CO luminosities (or molecular gas content, assuming the same α). Figs 3(C) and (D) show that at low $z < 0.1$, all quasars with CO measurements are QSO1. In general they have lower $L'_{\rm CO}$ and (for objects with $L_{\rm FIR}$ available) also lower $L_{\rm FIR}$ than LIRGs at similar z and ULIRGs in

[3] Due to the uncertainty regarding the CO detection in SDSS J0236+00, we will use the $L'_{\rm CO}$ upper limit in the discussion that follows.

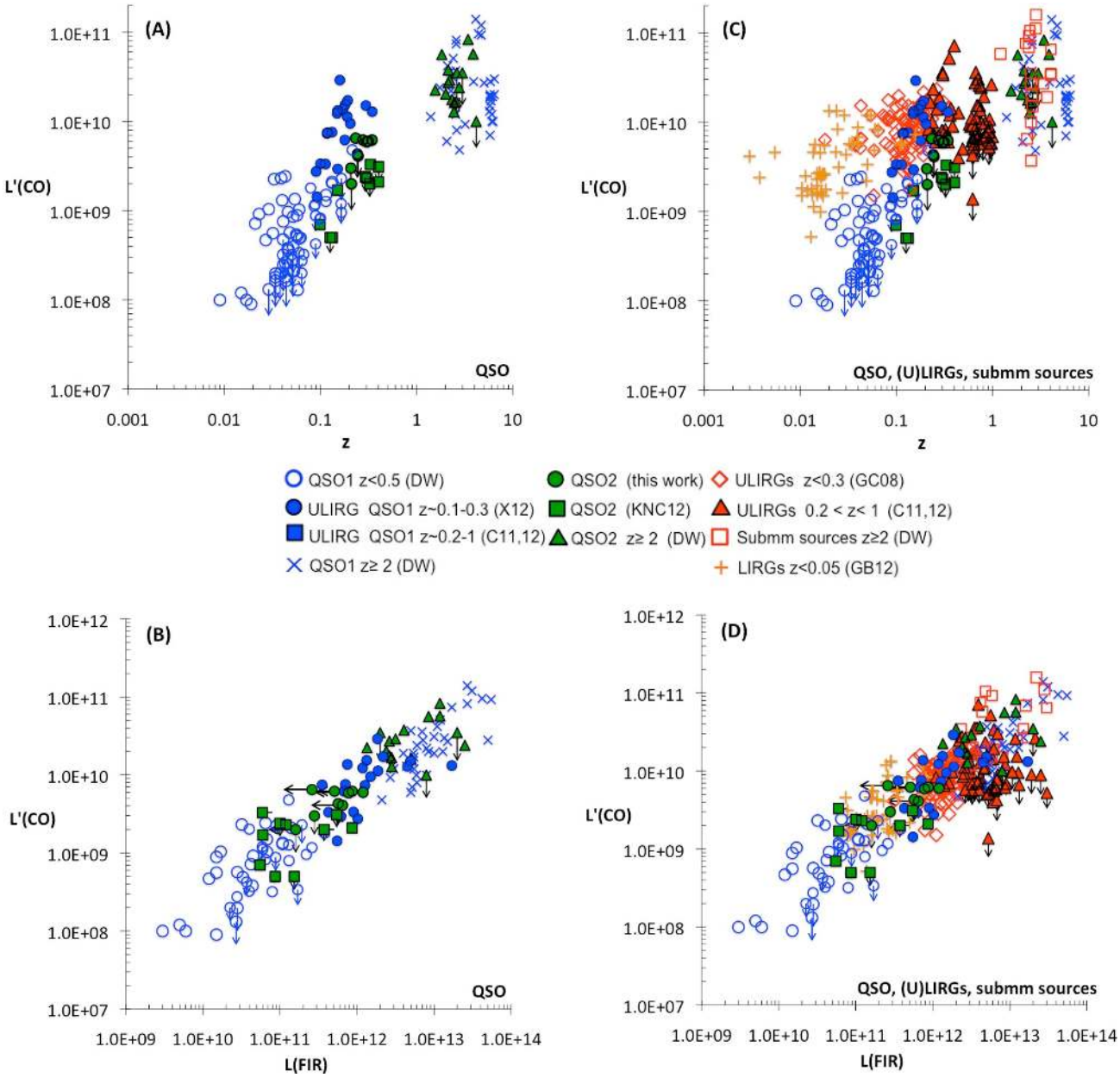

Figure 3. L'_{CO} versus z (left) and L'_{CO} versus L_{FIR} (right). The left-hand panels show only quasars: type 1 (blue symbols) and type 2 (green symbols). LIRGs (orange crosses) and ULIRGs (red symbols) (no quasars included in these samples) and high-z submm sources with no evidence for an AGN are added on the right-hand panels. References: DW (different works); X12 (Xia et al. 2012); C11 (Combes et al. 2011); C12 (Combes et al. 2012); KNC12 (Krips, Neri & Cox 2012); GB (Graciá Carpio et al. 2008); GC12 (García Burillo et al. 2012).

general. The scarcity of low-z QSO1 with high L_{FIR} luminosities in the LIRG regime or higher suggests that they are intrinsically different from more distant quasars ($z > 0.1$) in the diagrams. It is not clear what the difference is. Maybe the increasing incidence of major versus minor mergers as z and/or L_{FIR} increases.

Let us focus on the $z \sim 0.1$–0.4 range covered by the QSO2 sample. We have enlarged the total sample of quasars studied at this intermediate z by KNC12 with 19 ULIRG QSO1 from Xia et al. (2012) (blue solid circles in Fig. 2) and our 10 QSO2 (green solid circles).

We find that the 20 QSO2 observed so far at intermediate z fall on the L'_{CO} versus z and L'_{CO} versus L_{FIR} correlations. KNC12 found a trend for QSO2 to have lower L'_{CO} values than QSO1 at similar $z \sim 0.1$–0.4 (Fig. 3A). Adding our sample and the ULIRG QSO1 at similar z demonstrates that this difference is a consequence of their lower infrared luminosities. The L'_{CO} median values for our and KNC12 samples are $L'_{CO}{}^{med} \sim 6.0 \times 10^9$ and $\sim 2.3 \times 10^9$ K km s^{-1} pc^2, respectively, taking into account the upper limits. On the other hand, $L_{FIR}{}^{med} \sim 10^{11}$ L$_\odot$ for KNC12. $L_{FIR}{}^{med}$ is rather uncertain for our sample given the numerous upper limits. However, considering different realistic scenarios about the possible range of values (Wu et al. 2010), $L_{FIR}{}^{med} > 10^{11}$ L$_\odot$ is always found. Thus, our sample contains more luminous infrared sources, which explains the higher $L'_{CO}{}^{med}$. This is on the other hand somewhat surprising, since most objects in KNC12 are 24 μm selected sources, while our sources were selected in the optical from the SDSS QSO2 data base. Some unknown bias (e.g. maybe warmer or less obscured sources in KNC12) is possibly at work.

Table 4. Comparison of $L_{\rm FIR}$ and $L'_{\rm CO}$ between QSO2, QSO1, LIRGs and ULIRGs at $z \lesssim 0.1$–0.4 (data for LIRGs at $z > 0.05$ are very scarce). Nr. is the number of objects in each sample. It is found that samples with similar ${L_{\rm FIR}}^{\rm med}$ have similar ${L'_{\rm CO}}^{\rm med}$. For a given $L_{\rm FIR}$, no distinction is found between QSO1 and QSO2.

Object class	Nr.	z range	$z^{\rm med}$	${L_{\rm FIR}}^{\rm med}$ $\times 10^{11}$	${L'_{\rm CO}}^{\rm med}$ $\times 10^{9}$
QSO2	20	0.1–0.4	0.28	2.0	2.0
Non-ULIRG QSO1	8	0.1–0.2	0.15	1.8	1.2
ULIRGs QSO1	19	0.1–0.3	0.15	11.9	9.5
LIRGs	50	0.003–0.05	0.017	2.1	3.0
ULIRGs	103	0.1–0.4	0.17	19.4	8.9

The influence of $L_{\rm FIR}$ is also clear in Table 4 where we compare ${L'_{\rm CO}}^{\rm med}$ and ${L_{\rm FIR}}^{\rm med}$ for different samples of QSO1, QSO2, LIRGs and ULIRGs at $z \lesssim 0.4$. It can be seen that samples with similar ${L_{\rm FIR}}^{\rm med}$ have also similar $L'_{\rm CO}$.

Thus, for a fixed $L_{\rm FIR}$, QSO1 and QSO2 at $z \sim 0.1$–0.4 are indistinguishable regarding their molecular gas content, assuming the same conversion factor α applies. Comparison with (U)LIRGs reinforces that differences in $L'_{\rm CO}$ are a consequence of variations in $L_{\rm FIR}$. Although the QSO2 sample is affected by small number statistics, this result, if confirmed, is consistent with the unification model of QSO1 and QSO2.

To perform a more complete and adequate comparison between QSO1 and QSO2 it is essential to expand this study in z and $L_{\rm FIR}$, for both QSO1 and very specially QSO2. The low z ($z < 0.1$) range of QSO2 is completely unexplored, as well as the ULIRG regime at intermediate z. Similarly, it will be useful to enlarge the sample of non-ULIRG QSO1 at $z > 0.2$ to ensure an overlap on both z and $L_{\rm FIR}$ with the QSO2 samples.

We show in Fig. 4 (top) $L'_{\rm CO}$ versus $L_{\rm FIR}$ only for quasars (blue squares for QSO1 and green circles for QSO2), excluding upper limits for coherence with other works. A non-linear relation $L'_{\rm CO} \propto {L_{\rm FIR}}^{0.68\pm0.10}$ (black solid line) is found for the QSO1 and QSO2 combined sample (black solid line). The correlation coefficient R^2 is 0.89. The fit is consistent with the best-fitting power-law slope found by other authors (Xia et al. 2012; KNC12). When differentiating QSO2 and QSO1, the slopes are 0.66 and 0.70, respectively, well within the scatter, so it cannot be said whether a real difference is present. At the highest $L_{\rm FIR} > 10^{12}\,{\rm L}_{\odot}$ QSO2 seem to lie above QSO1. This difference is also apparent when including the upper limits for both object classes (Fig. 3B). However, most of these objects are at high z, and the measured values are affected by large uncertainties in general and poor statistics for QSO2. Thus, it is not clear that the difference is real. This further reinforces the interest of exploring the highest $L_{\rm FIR}$ regime for QSO2 at different z.

As already found by Xia et al. (2012), no dependence is found for the $L'_{\rm CO}$ versus $L_{\rm FIR}$ slope with $L_{\rm FIR}$. Gao & Solomon (2004) found that the slope for samples of low-luminosity star-forming galaxies, LIRGs and ULIRGs becomes steeper as the infrared luminosity increases (the scatter in our samples of ULIRGs and LIRGs is very large and the change of slope might be masked). This change of slope has been widely discussed in the literature. Different works propose that this is due to a variation of the relative ratio between the densest molecular gas, responsible for forming stars (traced at least in low $L_{\rm FIR}$ systems by HCN) and the less dense CO emitting gas (Gao & Solomon 2004; García Burillo et al. 2012).

We have computed $\eta = \frac{L_{\rm FIR}}{L'_{\rm CO}}$. It is used as a tracer of the star formation efficiency (SFE $= \frac{L_{\rm FIR}}{M_{\rm H2}}$) in objects where the IR luminosity is dominated by starbursts. If there is a significant contribution of the AGN to $L_{\rm FIR}$ in quasars, then η gives an upper limit on the SFE. On the other hand, different works show that using the HCN luminosity instead of $L'_{\rm CO}$ results in more reliable *SFE* values at least for non-ULIRG systems (Gao & Solomon 2004; Graciá Carpio et al. 2006; García Burillo et al. 2012). Therefore, the interpretation of η when comparing different samples is not trivial. However, provided these caveats are taken into account, the exercise can provide useful information, at least to constrain the exact role of such caveats.

η versus $L_{\rm FIR}$ is shown for quasars in Fig. 4 (middle). In this case, the vertical axis does not depend on the distance. LIRGs (orange crosses) and also ULIRGs and high-z submm sources (all represented with red diamonds) are added in Fig. 4 (bottom). Objects with upper limits for $L_{\rm FIR}$ and $L'_{\rm CO}$ have been eliminated as above. Clearly η correlates with $L_{\rm FIR}$ (as widely discussed in the literature; e.g. Gao & Solomon 2004; Xia et al. 2012). Although the number of QSO2 is small, they also follow this trend (middle panel). At high $L_{\rm FIR} > 10^{12}\,{\rm L}_{\odot}$, QSO2 apparently tend to lie below QSO1, but see warning above.

The trend defined by QSO overlaps with that defined by LIRGs and ULIRGs. At a given $L_{\rm FIR}$, there is no clear shift of the QSO towards higher η values relative to other samples of similar $L_{\rm FIR}$. Such a shift could be expected if the $L_{\rm FIR}$ is contaminated by dust emission heated by the AGN. However, the scatter is so large that the increase in η might be masked. Alternatively, such contamination might be negligible and thus, QSO would have similar star formation efficiencies than LIRGs or ULIRG of similar infrared luminosities.

5.3 CO kinematics

CO(1–0) has FWHM$_{\rm CO} \sim 180$–$370\,{\rm km\,s^{-1}}$ when detected (Table 2) in our QSO2 sample, using the FWHM inferred from one-Gaussian fits to the CO(1–0) line for all objects.[4] These values are consistent with KNC12 who measured FWHM$_{\rm CO}$ in the range $\sim$170–300 km s^{-1}. SDSS J1344+05 and SDSS J0025−10 (Villar-Martín et al. 2013) show evidence of double horned line profiles, which indicates a diversity of kinematic profiles. Double peaked CO lines have been found frequently in different types of galaxies, including QSO1, radio galaxies, (U)LIRGs and high-z submm galaxies (e.g. Evans et al. 2005; Narayanan et al. 2006; Bertram et al. 2007; Daddi et al. 2010; Ocaña Flaquer et al. 2010). Rotation is most frequently claimed to explain them, although an alternative explanation is mergers. This is the case of SDSS J0025−10 (Villar-Martín et al. 2013). In this double nuclei merging system, one of the two CO

[4] For the double horned profiles of SDSS J1344+05 and SDSS J0025−10, one-Gaussian fits produce FWHM $= 300 \pm 40$ and 265 ± 20 km s^{-1}, respectively.

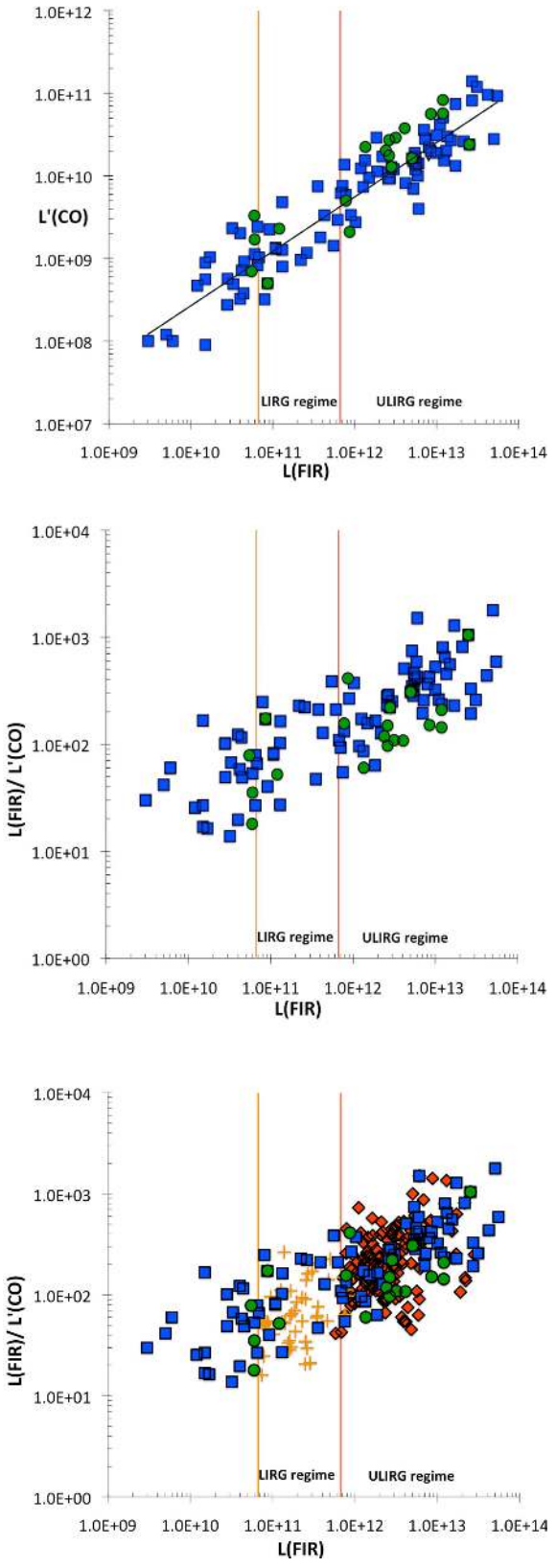

Figure 4. L'_{CO} versus L_{FIR} (top) for the QSO1 (blue squares) and QSO2 (green circles) in Fig. 3. Upper limits have been excluded. $\eta = \frac{L_{FIR}}{L'_{CO}}$ versus L_{FIR} only for quasars (middle). LIRGs (orange crosses) and ULIRGs and high-z submm sources (all represented with red diamonds) are added in the bottom panel. The approximate separation between the different infrared luminosity regimes is indicated with vertical lines.

Table 5. Comparison of CO(1–0) FWHM for QSO2 (this work and KNC12), ultraluminous QSO1 (Xia et al. 2012) and other QSO1 from different samples. Notice that the L_{FIR} values might vary relative to Table 4 because here we only consider objects with CO(1–0) FWHM measurements. The QSO samples are separated by a horizontal line from (U)LIRGs.

Object class	z^{med}	Nr.	$FWHM_{CO}^{med}$ km s^{-1}	${L_{FIR}}^{med}$ $\times 10^{11} L_{\odot}$
QSO2	0.30	10	280	2
Non-ULIRG QSO1	0.06	34	223	0.6
ULIRG QSO1 Xia12	0.15	17	275	11.9
LIRGs	0.02	18	253	1.4
ULIRG	0.14	91	304	16.0

kinematic component is associated with the QSO nucleus and/or the intermediate region between the companion nuclei. The other CO component is associated with the northern tidal tail, including a tidal dwarf galaxy on its tip.

In general, we find that the CO line is narrower than [O III]λ5007, with $\frac{FWHM_{[O\,III]}}{FWHM_{CO}} \sim 1$–2 (see Table 2). This effect is also observed in low-z QSO1 (e.g. Shields et al. 2006). The difference in FWHM probably reveals different spatial sizes and geometry of the ionized and molecular phases and a higher sensitivity of the [O III] emission to non-gravitational motions, such as outflows. Indeed Greene & Ho (2005) find that $FWHM_{[O\,III]}$ is in general broader than that of the stars $FWHM_{*}$ in a large sample of type 2 AGNs within a broad [O III] luminosity range ($\sim$ 3 orders of magnitude, including objects with $\log(L_{[O\,III]}) > 8.3$ typical of quasars; see Section 2).

We show in Table 5 $FWHM_{CO}$ (median values) for all the samples with available data at $z \lesssim 0.5$,[5] together with the median values of z and L_{FIR} (notice that these can vary relative to Table 4, since here we consider sub-samples with FWHM data and $z \lesssim 0.5$). All samples show relatively similar $FWHM_{CO}^{med}$, in spite of the difference in L_{FIR}. On the other hand, a trend is hinted for larger FWHM at the highest L_{FIR} and smaller FWHM at the lowest L_{FIR}.

$FWHM_{CO}^{med}$ is plotted versus L_{FIR} in Fig. 5 for the individual sources. The same symbols as in Fig. 3 are used, except that now all QSO2 (KNC12 and our sample) are represented with green solid circles. There is no correlation between $FWHM_{CO}$ and L_{FIR}, but similar trends as in Table 5 are hinted. The broadest lines ($FWHM_{CO}^{med} > 400$ km s^{-1}) are in general only in ULIRGs, i.e. in the high L_{FIR} regime. On the other hand, those objects with the lowest L_{FIR} ($\lesssim$several $\times\ 10^{10}\ L_{\odot}$) tend to be associated with narrower CO lines. QSO2 shows a range of linewidths in the same range as LIRGs (they also have similar L_{FIR}). The difference might point to the larger incidence of galaxy mergers/interactions at the highest L_{FIR}, as suggested by the fact that all ULIRGs show signatures of strong interactions and mergers (Sanders & Mirabel 1996).

If we focus on the $z \sim 0.1$–0.4 range spanned by the QSO2 sample, the range and median value of $FWHM_{CO}$ of all 10 QSO2 with available data are similar to that of QSO1 at similar z. In the unification scheme of QSO1 and QSO2, this result suggests that the CO emitting gas is not coplanar with the obscuring torus. If this was the case, the FWHM would depend on the inclination and thus the type 1 versus type 2 orientation (see also KNC12). On the other hand, it is not clear what role selection effects are playing, since

[5] In those cases where only the FWZI is provided (Bertram et al. 2007; Scoville et al. 2003), the ratio FWZI/FWHM = 1.9 has been assumed. For comparison, the QSO1 in Xia et al. (2012) sample has ratios in the range ∼1.4–2.5 with a median value of 1.9.

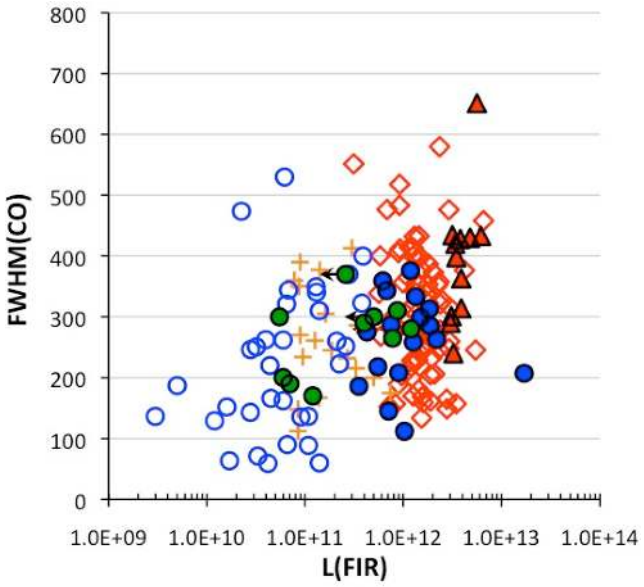

Figure 5. $FWHM_{CO(1-0)}$ in km s^{-1} versus L_{FIR} for all samples at $z \lesssim 0.5$. Symbols as in Fig. 3 except that all QSO2 (KNC12 and this work) are now represented with green solid circles.

CO signals with narrower FWHM are generally easier to detect for a given L'_{CO} and velocity resolution.

$FWHM_{CO}$ has been often used as a tracer of dynamical masses in different systems, including quasars (e.g. Bothwell et al. 2013). However, the finding of large reservoirs of molecular gas shifted spatially from the quasar nucleus and associated with companion objects or tidal features shows that this is not always valid (e.g. Aravena et al. 2008; Papadopoulos et al. 2008; Villar-Martín et al. 2013; see also Bothwell et al. 2013 for a discussion). It is first essential to characterize accurately both the kinematics and spatial distribution (size, geometry) of the molecular gas.

6 SUMMARY AND CONCLUSIONS

We present results of CO(1–0) spectroscopic observations of 10 SDSS type 2 quasars at $z \sim 0.2$–0.3 observed with the 30-m IRAM radio telescope and the ATCA. With our work, the total number of QSO2 with CO observations at $z < 1.5$ increases to ∼20, all of which are at $0.1 \lesssim z \lesssim 0.4$.

We report five new confirmed CO(1–0) detections and one tentative detection for our QSO2 sample. They have $L'_{CO} \sim$ several $\times$ 10^9 K km s^{-1} pc^2, while upper limits for the non-detections are $L'_{CO} < 3\sigma =$ several $\times$ 10^9 K km s^{-1} pc^2. Assuming a conversion factor $\alpha = 0.8$, and including the sample studied by KNC12, the implied molecular gas masses for the 20 QSO2 with CO observations at $z \sim 0.1$–0.4 are in the range $M_{H_2} \lesssim 4 \times 10^8$ to $\sim 5 \times 10^9$ M$_\odot$.

We have constrained the L_{IR} and L_{FIR} of our sample by fitting the mid- to far-infrared SEDs. The L_{IR} and L_{FIR} values of KNC12 sample have also been constrained more accurately. Most QSO2 (17/20) are in the LIRG regime or below with $L_{IR} < 10^{12}$ L$_\odot$. The remaining three have $L_{IR} \sim 10^{12}$ L$_\odot$, in the transition between the LIRG and ULIRG regimes. A more complete characterization of the molecular gas content of QSO2 at similar z requires to expand this study to the highest $L_{IR} \gtrsim$ several $\times$ 10^{12} L$_\odot$. Larger molecular gas reservoirs $M_{H_2} > 10^{10}$ M$_\odot$ will most probably be found.

We have been able to constrain the L_{IR}/L_{FIR} ratios for nine QSO2. In all cases, this value is in the range ∼1.4–1.7 with a median value of 1.5, which is lower than ratios typical of QSO1. This is consistent with a higher obscuration of the mid-infrared luminosity in QSO2 compared to QSO1 as expected.

At intermediate z no difference is found on L'_{CO} (or the molecular gas content) between QSO2 and QSO1 once the infrared luminosities are accounted for. This is consistent with the unification model of QSO1 and QSO2.

QSO2 fall on the L'_{CO} versus z, L'_{CO} versus L_{FIR} and $\eta = \frac{L_{FIR}}{L'_{CO}}$ versus L_{FIR} correlations defined by quasars at different z. The location of the QSO2 in these diagrams is discussed in comparison with samples of QSO1, LIRGs, ULIRGs and high-z submm sources.

CO(1–0) has $FWHM_{CO} \sim 180$–370 km s^{-1} when detected, with a variety of kinematic profiles (single or double horned). In our sample, the CO line is in general narrower than the [O III]λ5007, as observed in low-z QSO1. This probably reveals different spatial sizes and geometry of the ionized and molecular phases and a higher sensitivity of the [O III] emission to non-gravitational motions, such as outflows. The range and median value of $FWHM_{CO}$ of all 10 QSO2 with available data are similar to that of QSO1 at similar z, although this result is tentative. In the unification scenario of QSO1 and QSO2 this result, if confirmed, suggests that the spatial distribution of the CO(1–0) emitting gas is not related to the obscuring torus and is therefore independent of its orientation relative to the observer.

To perform a more complete and adequate comparison between QSO1 and QSO2 it is essential to expand this study in z and L_{FIR}, for both QSO1 and very specially QSO2. The low-redshift ($z < 0.1$) range is completely unexplored for low-z QSO2, as well as the ULIRG regime at intermediate z. Similarly, it will be useful to enlarge the sample of non-ULIRG QSO1 at $z > 0.2$ to ensure an overlap on both z and L_{FIR} with the QSO2 samples.

ACKNOWLEDGEMENTS

This work has been funded with support from the Spanish former Ministerio de Ciencia e Innovación through the grant AYA2010-15081. MR acknowledges support by the Spanish MINECO through grant AYA 2012-38491-C02-02, cofunded with FEDER funds. Thanks to the staff at IRAM Pico Veleta for their support during the observations. IRAM is supported by INSU/CNRS (France), MPG (Germany) and IGN (Spain). The Australia Telescope is funded by the Commonwealth of Australia for operation as a National Facility managed by CSIRO. This research has made use of the VizieR catalogue access tool (CDS, Strasbourg, France) and the NASA/IPAC Extragalactic Database (NED).

The SDSS spectra and images of the sample have been used for different issues essential to the paper. Funding for the SDSS and SDSS-II has been provided by the Alfred P. Sloan Foundation, the Participating Institutions, the National Science Foundation, the U.S. Department of Energy, the National Aeronautics and Space Administration, the Japanese Monbukagakusho, the Max Planck Society and the Higher Education Funding Council for England. The SDSS Web Site is http://www.sdss.org/. The SDSS is managed by the Astrophysical Research Consortium for the Participating Institutions.

REFERENCES

Aravena M. et al., 2008, A&A, 4191, 173

Bertram T., Eckart A., Fischer S., Zuther J., Straubmeier C., Wisotzki L., Krips M., 2007, A&A, 470, 571

Bessiere P., Tadhunter C., Ramos Almeida C., Villar Martín M., 2012, MNRAS, 426, 276

Bothwell M. et al., 2013, MNRAS, 429, 3047
Briggs D. S., 1995, PhD thesis, New Mexico Tech
Carilli C. et al., 2002, AJ, 123, 1838
Carilli C. et al., 2010, ApJ, 714, 1407
Combes F., 1991, ARA&A, 29, 195
Combes F., García Burillo S., Braine J., Schinnerer E., Walter F., Colina L., 2011, A&A, 528, 124
Combes F., García Burillo S., Braine J., Schinnerer E., Walter F., Colina L., 2012, A&A, 550, 41
Coppin K. et al., 2008, MNRAS, 389, 45
Cox P. et al., 2002, A&A, 387, 406
Daddi E. et al., 2009, ApJ, 694, 1517
Daddi E. et al., 2010, ApJ, 713, 686
De Breuck C., Downes D., Neri R., van Breugel W., Reuland M., Omont A., Ivison R., 2005, A&A, 130, 1
di Serego Alighieri S., Cimatti A., Fosbury R., Hes R., 1997, A&A, 328, 510
Downes D., Solomon P., 1998, ApJ, 507, 615
Drouart G. et al., 2012, A&A, 548, 45
Emonts B. et al., 2011a, ApJ, 734, L25
Emonts B. et al., 2011b, MNRAS, 415, 655
Evans A. S., Frayer D. T., Surace J. A., Sanders D. B., 2001, AJ, 121, 1893
Evans A., Mazzarella J., Surace J., Frayer D., Iwasawa K., Sanders D., 2005, ApJS, 159, 197
Evans A. S., Solomon P. M., Tacconi L., Vavilkin T., Downes D., 2006, AJ, 132, 2398
Gao Y., Solomon P., 2004, ApJ, 606, 271
Gao Y., Carilli C., Solomon P., Vanden Bout P., 2007, ApJ, 660, 93
García-Burillo S., Usero A., Alonso-Herrero A., Graciá-Carpio J., Pereira-Santaella M., Colina L., Planesas P., Arribas S., 2012, A&A, 539, 8
Graciá Carpio J., García-Burillo S., Planesas P., Colina L., 2006, ApJ, 640, L135
Graciá Carpio J., García-Burillo S., Planesas P., Fuente A., Usero A., 2008, A&A, 479, 703
Greene J., Ho L., 2005, ApJ, 627, 721
Greene J., Zakamska N., Liu X., Barth A., Ho L., 2009, ApJ, 702, 441
Greene J., Zakamska N., Ho L., Barth A., 2011, ApJ, 732, 9
Guilloteau S., Forveille T., 1989, Grenoble Image and Line Data Analysis System (GILDAS), Saint Martin d'Hres, IRAM, available at http://www.iram.fr/IRAMFR/GILDAS
Heckman T., Kauffmann G., Brinchmann J., Charlot S, Tremonti C., White S., 2004, ApJ, 613, 109
Hiner K., Canalizo G., Lacy M., Sajina A., Armus L., Ridgway S., Storrie Lombardi L., 2009, ApJ, 706, 508
Hopkins A., Beacom J., 2006, ApJ, 651, 142
Humphrey A., Villar-Martín M., Snchez S. F., Mart'nez-Sansigre A., González Delgado R., Pérez E., Tadhunter C., Pérez-Torres M. A., 2010, MNRAS, 408, L1
Ivison R., Papadopoulos P., Smail I., Greve T., Thomson A., Xilouris E., Chapman S., 2011, MNRAS, 412, 1913
Keres D., Min S., Young J., 2003, ApJ, 582, 659
Krips M. et al., 2005, A&A, 439, 75
Krips M., Neri R., Cox P., 2012, ApJ, 753, 135 (KNC12)
Lacy M., Sajina A., Petric A., Seymour N., Canalizo G., Ridgway E., Armus L., Sotrrie-Lombardi L., 2007, ApJ, 669, L61
Lacy M., Petric A., Mart'nez-Sansigre A., Ridgway S., Sajina A., Urrutia T., Farrah D., 2011, AJ, 142, 196
Lagos C., Baugh C., Lacey C., Benson A., Kin H-S, Power C., 2011, MNRAS, 418, 1649
Maiolino R. et al., 2007, A&A, 472, L33
Martínez-Sansigre A., Rawlings S., Lacy M., Fadda D., Jarvis M., Marleau F., Simpson C., Willott C., 2006, MNRAS, 370, 1479
Martínez-Sansigre A. et al., 2009, ApJ, 706, 184
Middelberg E., Sault R., Kesteven M., 2006, Publ. Astron. Soc. Aust., 23, 147
Miley G., de Breuck C., 2008, A&AR, 15, 67
Miller L., Peacock J., Mead A., 1990, MNRAS, 244, 207
Narayanan W., Groppi C., Kulesa C., Walker C., 2006, ApJ, 642, 616
Neri R. et al.2003, ApJ, 597, L113
Ocaña Flaquer B., Leon S., Combes F., Lim J., 2010, A&A, 518, 9
Omont A., 2007, Rep. Prog. Phys., 70, 1099
Papadopoulos P., Ivison R., Carilli C., Lewis G., 2001, Nat, 409, 58
Papadopoulos P., Feain I., Wagg J., Wilner D., 2008, ApJ, 648
Papadopoulos P., van der Werf P., Xilouris E., Isaak K., Gao Y., 2012, ApJ, 751, 10
Patton D., Carlberg R., Marzke R., Pritchet C., da Costa L., Pellegrini P., 2000, ApJ, 536, 153
Pérez González E. et al., 2005, ApJ, 630, 82
Polletta M. et al., 2007, ApJ, 663, 81
Polletta M., Nesvadba N., Neri R., Omont A., Berta S., Bergeron J., 2011, A&A, 533, 20
Pott J. U., Eckart A., Krips M., Tacconi-Garman L. E., Lindt E., 2006, A&A, 456, 505
Reyes R. et al., 2008, AJ, 136, 2373
Riechers D., 2011, ApJ, 730, 108
Riechers D. et al., 2006, ApJ, 650, 604
Riechers D., Walter F., Frank B., 2009a, ApJ, 703, 1338
Riechers D., Walter F., Carilli C., Lewis G., 2009b, ApJ, 690, 485
Sage L. S., 1990, A&A, 239, 125
Sanders D. B., Mirabel F., 1996, ARA&A, 34, 749
Sanders D. B., Phinney E., Neugebauer G., Soifer B., Matthews K., 1989, ApJ, 347, 29
Schumacher H., Martínez Sansigre A., Lacy M., Rawlings S., Schinnerer E., 2012, MNRAS, 423, 2132
Scoville N., Frayer D., Schinnerer E., Christopher M., 2003, ApJ, 585, L105
Shields G., Menezes K., Massart C., Vanden Bout P., 2006, ApJ, 641, 683
Smail I., Smith G., Ivison R., 2005, ApJ, 631, 121
Solomon P., Vanden Bout P., 2005, ARA&A, 43, 677
Solomon P., Downes D., Radford S., 1992, ApJ, 389, L29
Stanford S., Stern D., van Breugel W., De Breuck C., 2000, ApJS, 131, 185
Stern D. et al., 2005, ApJ, 631, 163
Szokoly G et al., 2004, ApJS, 144, 271
Tacconi L. et al., 2010, Nat, 463, 781
Vernet J., Fosbury R., Villar-Mart'n M., Cohen M., Cimatti A., di Serego Alighieri S., Goodrich R., 2001, A&A, 366, 7
Villar-Martín M., Tadhunter C., Humphrey A., Fraga Encina R., González Delgado R., Pérez Torres M., Martínez-Sansigre A., 2011a, MNRAS, 416, 262 (VM11a)
Villar-Martín M., Humphrey A., González Delgado R., Colina L., Arribas S., 2011b, MNRAS, 418, 2032
Villar-Martín M., Cabrera Lavers A., Bessiere P., Tadhunter C., Rose M., de Breuck C., 2012, MNRAS, 423, 80
Villar-Martín M., Emonts B., Rodríguez M., Pérez Torres M., Drouart G., 2013, MNRAS, 432, 2104
Walter F., Carilli C., Bertoldi F., Menten K., Cox P., Lo K., Fan X., Strauss M., 2004, ApJ, 615, L17
Wang R. et al., 2010, ApJ, 714, 699
Wang R. et al., 2011, AJ, 142, 101
Weiss A., Downes D., Walter F., Henkel C., 2005, A&A, 440, L45
Wu Y. et al., 2010, ApJ, 723, 895
Xia X. Y. et al., 2012, ApJ, 750, 92
Yan L. et al., 2010, ApJ, 714, 100
York D. G. et al., 2000, AJ, 120, 1579
Zakamska N. et al., 2003, AJ, 126, 2125
Zakamska N. et al., 2005, AJ, 129, 1212
Zakasmka N., Gómez L., Strauss M., Krolik J., 2008, ApJ, 136, 1607

APPENDIX A: FITS OF THE SPECTRAL ENERGY DISTRIBUTIONS

The figures with the mid-(WISE; 3.3, 4.6, 11.6, 22.1 μm) to far-infrared (*IRAS*; 60 and/or 100 μm) photometric data and the SED fits for our sample are shown here. The solid diamonds correspond to the detected fluxes, while open triangles indicate upper limits. When two values appear at $\lambda \sim 22$–25 μm, these correspond to the WISE 22.1 μm and *IRAS* 25 μm bands. See Section 4.3 for more detailed information.

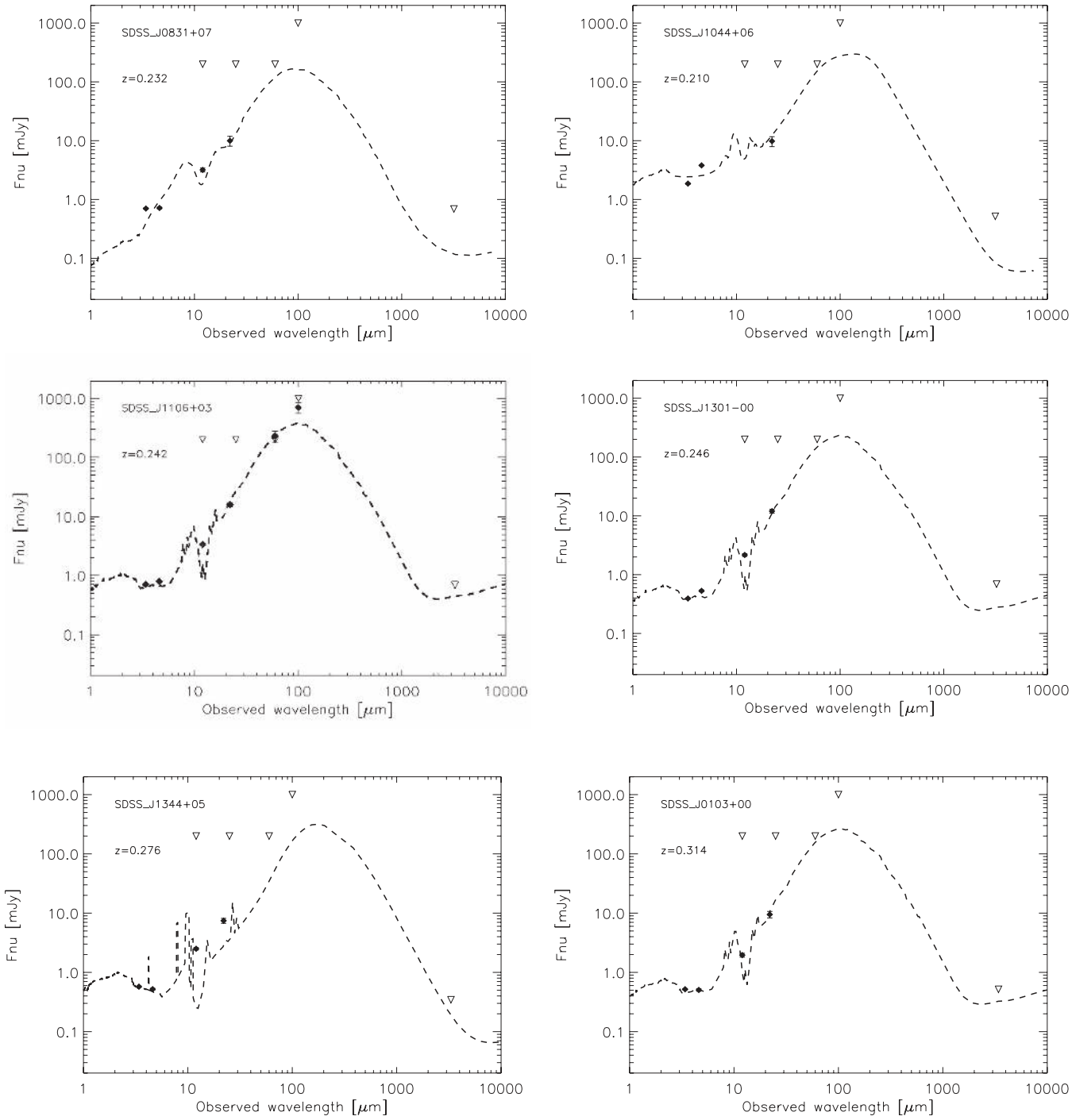

Figure A1. Fits of the infrared SEDs of the QSO2 in our sample. Detections and upper limits are shown with solid diamonds and open triangles, respectively. For those objects with no detections at far-infrared wavelengths (60 and/or 100 μm) only upper limits for L_{IR} and L_{FIR} could be established. For these, the fits producing the maximum possible L_{IR} consistent with the mid-infrared photometry and the far-infrared upper limits are shown.

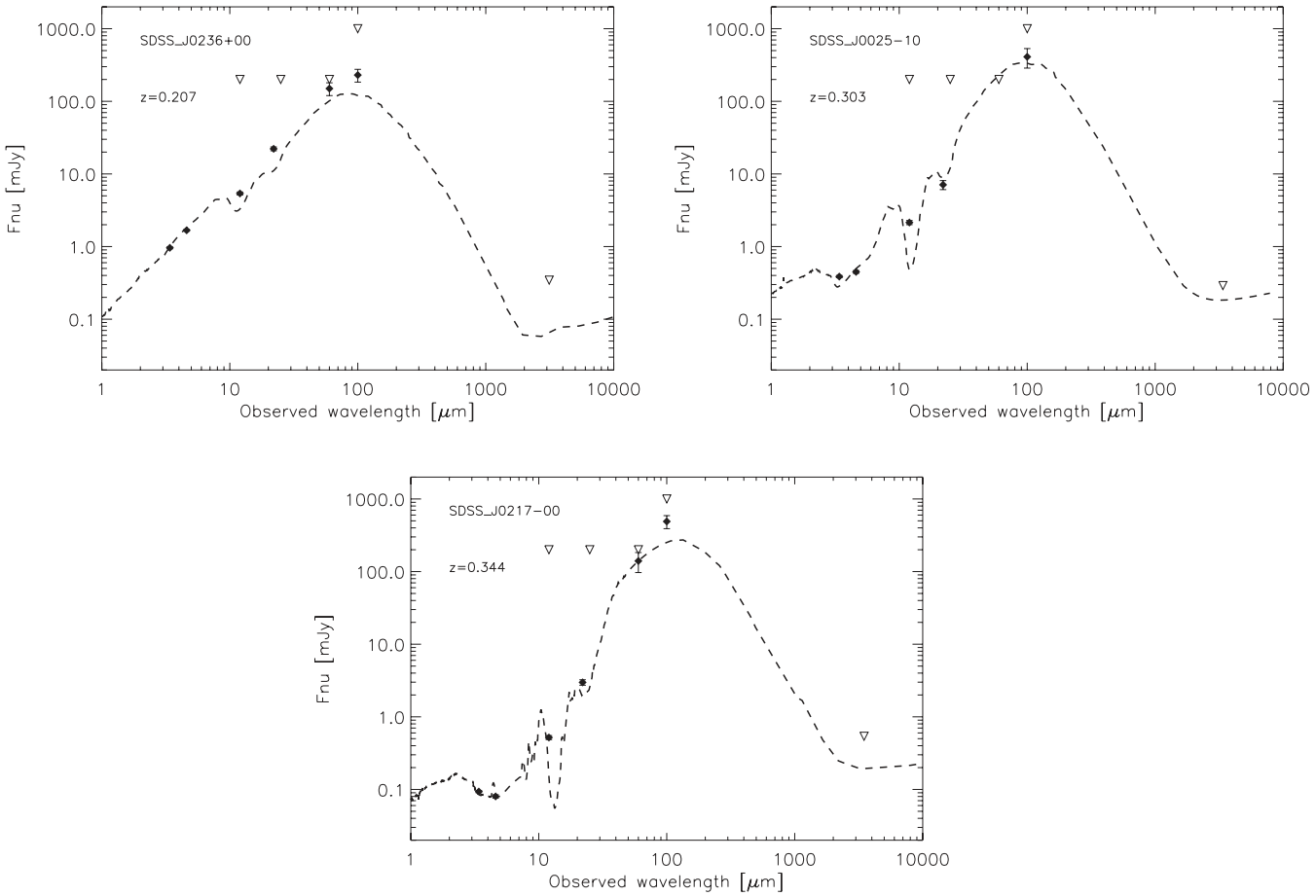

Figure A1 – *continued*

This paper has been typeset from a TEX/LATEX file prepared by the author.